
NGM-SLAM: Gaussian Splatting SLAM with Neural Radiance Field Submap

Mingrui Li¹, Jingwei Huang^{2*}, Lei Sun³, Aaron Xuxiang Tian⁴, Tianchen Deng⁵, Shuhong Liu⁶,

Guangan Jiang¹, Hongyu Wang^{1*}

¹Dalian University of Technology

²University of Electronic Science and Technology of China

³University of Pennsylvania

⁴Carnegie Mellon University

⁵Shanghai Jiaotong University

⁶The University of Tokyo

2905450254@mail.dlut.edu.cn

Abstract

SLAM systems based on Gaussian Splatting have garnered attention due to their capabilities for rapid real-time rendering and high-fidelity mapping. However, current Gaussian Splatting SLAM systems usually struggle with large scene representation and lack effective loop closure detection. To address these issues, we introduce NGM-SLAM, the first 3DGS based SLAM system that utilizes neural radiance field submaps for progressive scene expression, effectively integrating the strengths of neural radiance fields and 3D Gaussian Splatting. We utilize neural radiance field submaps as supervision and achieve high-quality scene expression and online loop closure adjustments through Gaussian rendering of fused submaps. Our results on multiple real-world scenes and large-scale scene datasets demonstrate that our method can achieve accurate hole filling and high-quality scene expression, supporting monocular, stereo, and RGB-D inputs, and achieving state-of-the-art scene reconstruction and tracking performance.

1 Introduction

SLAM systems [1, 15–17, 37, 41] have long been a fundamental concern in the domains of robotics and AR/VR. Dense SLAM [6, 12, 19–21, 23], in particular, commands a broader range of applications and demand compared to its sparse counterparts. Traditional dense SLAM systems [33, 34] utilize explicit representations like voxels, point clouds, and TSDF [22], and have achieved commendable results in tracking. However, the limitations of traditional dense SLAM [38, 40] in high-fidelity modeling, gap filling, and texture details restrict their wider application.

Neural implicit SLAM, leveraging NeRF-based [24–26, 28] implicit representations, has crafted a complete pipeline that includes tracking and mapping, significantly enhancing the perceptual capabilities of SLAM systems[34]. Despite these advancements, current neural implicit SLAM systems face limitations in operational speed, real-time capabilities, and memory requirements. Recent developments in SLAM methods based on 3D Gaussian Splatting (3DGS) [29] not only retain the high-fidelity mapping benefits of NERF-SLAM systems but also demonstrate advantages in rendering speed and precision, challenging the dominant position of neural implicit SLAM in dense reconstruction. 3DGS employs continuous Gaussian characterized by color opacity and orientation for

*Use footnote for providing further information about author (webpage, alternative address)—not for acknowledging funding agencies.

scene representation, combining the intuitive flexibility of explicit representations with the continuous differentiability of implicit expressions.

However, it's notable that 3DGS, compared to NeRF [49–52], suffers from limitations in filling scene gaps, because it lacks the generalizing inference capabilities from neural networks. Additionally, compared to NeRF-SLAM system current 3DGS-SLAM systems lack robust loop detection, which is crucial for correcting global drift errors and preventing map loss. This disadvantage becomes particularly apparent in large scenes due to cumulative drift.

To address these challenges, we propose a SLAM system based on neural submaps and 3DGS representation. We first establish submaps represented by neural radiance fields and construct a global keyframe list. When triggering map thresholds, we create new neural submaps and use previous submaps as priors to guide Gaussian rendering. Subsequently, we perform local bundle adjustment (BA). Between submaps, we implement a submap fusion strategy and trim the generated submaps' Gaussians. Upon loop closure detection, we perform real-time coarse-to-fine global loop adjustments, adjusting the map poses corresponding to anchor frames and applying global BA and global Gaussian rendering loss to correct accumulated drift. We significantly mitigate errors caused by accumulated drift and map drift, while correcting global map loops with minimal computational overhead. Experimental results demonstrate that our method achieves state-of-the-art performance in tracking and mapping and is scalable to large-scale scenes. In summary, our contributions are as follows:

- We introduce the first progressive dense Gaussian splatting SLAM system based on neural submaps, achieving high-fidelity mapping through a local-to-global reconstruction strategy. We enable large-scale scene inference and effectively leverage the advantages of both representation methods.
- We propose a local-to-global loop detection and correction method that utilizes neural submaps to supervise 3DGS map rendering, enabling real-time correction of the system's accumulated errors.
- Our system supports monocular, stereo, and RGB-D inputs, demonstrating state-of-the-art tracking and mapping performance on 5 datasets, and supports real-time inference at 5 FPS in large-scale scenes.

2 Related Work

Dense Visual SLAM Dense real-time scene mapping is considered a key method for solving problems related to scene understanding, autonomous driving, and AR/VR applications [36]. Early methods like KinectFusion utilized an explicit scene representation approach to achieve comprehensive tracking and mapping, offering more accurate scene expression and geometric shapes compared to sparse point-based methods. Traditional dense SLAM systems extensively employ various explicit representations such as voxels and point clouds. The advantages of traditional dense SLAM methods lie in their accurate and mature tracking systems, but they have limitations in providing high-fidelity models and lack generalized reasoning capabilities.

Recent years have seen significant attention given to methods based on neural radiance fields [2–5]. iMAP [48] established the first complete neural implicit SLAM framework, achieving scalable and efficient scene representation. However, limitations due to a single MLP architecture can lead to tracking loss and mapping errors in larger-scale scenes. NICE-SLAM [1] utilizes a pretrained multi-MLP system with frozen parameters to achieve accurate tracking and scene expression, yet it faces drift issues in filling gaps. ESLAM [18] uses tri-plane features for scene representation, while Go-SLAM [54] supports multimodal inputs from monocular, stereo, and RGB-D cameras. However, these neural implicit methods [7] generally lack online loop closure correction. The use of MLP often resulting in the loss of high-frequency details due to local over-smoothing.

3D Gaussian Based SLAM Recently, 3DGS based scene representation methods have garnered broad interest. Compared to NeRF-based neural implicit methods [44–46], 3D Gaussian Splatting methods [43] combine the advantages of explicit and implicit expressions. They capture high-fidelity three-dimensional scenes through a differentiable rasterization process, avoiding the per-pixel ray casting required by neural fields, thus achieving high-speed rendering. Photo-SLAM [59] achieves high-quality real-time representation using a Gaussian pyramid-based approach. SplaTAM [5] employs

anisotropic Gaussian representation, achieving real-time tracking and rendering. MonoGS [4] achieves faster scene representation through Gaussian shape regularization and geometric verification, but lacks loop closure correction to eliminate accumulated errors. However, these methods face many challenges. Because 3D Gaussian Splatting (3DGS) representations cannot learn scene features for inference, they cannot fill gaps like NeRF-based methods. Furthermore, current 3DGS SLAM methods still lack stable and complete tracking systems, such as loop detection and online bundle adjustment (BA). We propose an incremental scene representation method that combines the strengths of NeRF and 3DGS for complementary scene expression—a method that can learn features while retaining complete high-frequency details. By establishing a neural implicit submap based on NeRF as a prior to guide 3D Gaussian rendering, our method can effectively fill gaps and achieve more comprehensive scene reconstruction. The use of multi-scale Gaussian rendering ensures optimized rendering speed and enhances local details. The online adjustment of our neural radiance field submap allows global BA without the need for re-rendering. Although our method adopts a hybrid rendering approach, our parallel submap tracking and optimization avoid the costs associated with global scene updates, thereby improving overall system speed.

3 Method

We present the system pipeline of NGM-SLAM in Figure 1. Our system first tracks and constructs submaps based on RGB/RGB-D image streams using neural radiation fields (Section 3.1). Then, the neural submaps are utilized to construct Gaussian priors supervised submaps (Section 3.2). To correct the drift errors we design a local-to-global loop closure detection and bundle optimization process (Section 3.3). Finally, we execute a submap fusion strategy with the aligned submap poses (Section 3.4). We will elaborate on the entire process of our system in the methodology section.

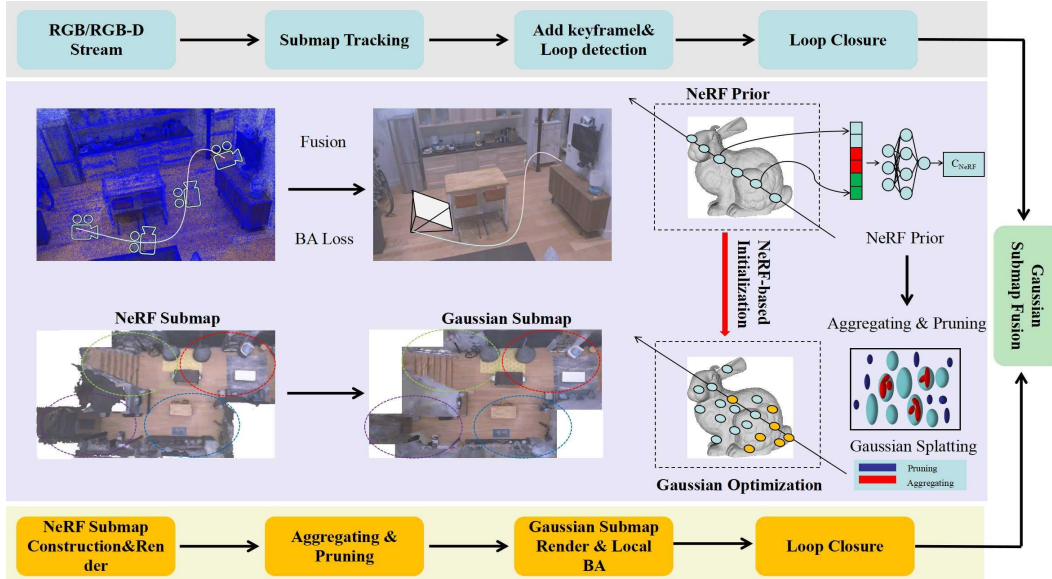


Figure 1: The system consists of two modules: tracking and mapping. After constructing the initial submap, the tracking module continuously estimates the camera pose and detects loops, while passing keyframes of the submap to the mapping module. The mapping module first constructs a neural submap, which also serves as a prior for the 3D Gaussian submap, and performs parallel rendering between submaps. Local bundle adjustment (BA) is performed within each submap to correct pose and mapping errors. When loop closure is detected, global BA is executed on all anchor frames (keyframes of the submaps), followed by BA on all keyframes of the submaps. Finally, the generated 3DGS maps are fused together.

3.1 Neural Submap Construction

Neural Submap Construction In current 3D Gaussian-based SLAM systems, due to the lack of generalized inferencing capabilities of neural networks, we have introduced data-driven, incremental

neural submaps as a foundational supervisory mechanism to fill voids and enhance map representation. Our approach is based on ORB feature point tracking [30], as feature point extraction is performed only on the current input frame, which avoids the frequent drift issues associated with submap creation and hole filling.

We establish a local submap list of keyframes and a global list of keyframes to initial the submap. This facilitates the effective implementation of local/global Bundle Adjustment (BA) processes. When tracking begins, the first frame of the local submap is simultaneously added to the local keyframes and global keyframes list. We set a keyframe threshold N for submaps; when a submap accumulates enough keyframes to reach this threshold, we establish a new local submap.

To better achieve map fusion and avoid excessive fusion errors between submaps, we utilize the DBOW model to assess the co-visibility relationships between keyframes. If the map connection frames lack co-visibility, the current submap's connecting frame is added as the first frame to a newly created submap to ensure stable map integration.

Neural Implicit Rendering Due to the speed of Gaussian rendering compared to NeRF, we adopt a progressive rendering strategy to achieve real-time rendering between submaps and the global map. We perform neural implicit rendering using only a sparse set of keyframes for each submap to obtain foundational supervision. Once the submap is preliminarily adjusted, full-frame poses are utilized for Gaussian rendering to refine the mapping process. To reduce the rendering cost, we employ a multi-resolution hash radiance field [50] as a prior.

The radiance field f is a continuous function that maps a three-dimensional point position $p \in \mathbb{R}^3$ and a viewing direction $d \in S^2$ to a volume density $\sigma \in \mathbb{R}_+$ and a NeRF RGB color value $\mathbf{C}_N \in \mathbb{R}^3$. Inspired by NeRF volume rendering, the final color prediction for a pixel is approximated through ray marching and integration using sample points:

$$\mathbf{C}_N = \sum_{j=1}^N T_{Nj} \alpha_j \mathbf{C}_j, \quad \text{where } T_{Nj} = \prod_{k=1}^{j-1} (1 - \alpha_k), \quad \alpha_j = 1 - e^{-\sigma_j \delta_j} \quad (1)$$

where T_{Nj} is the NeRF transmittance, α_j is the alpha value for x_j , and δ_j is the distance between adjacent sample points. In neural radiance fields, f is parameterized as an MLP with ReLU activation f_θ , and the network parameters θ are optimized via gradient descent on the reconstruction loss:

$$\mathcal{L}(\theta) = \sum_{\mathbf{r} \in \mathcal{R}_b} \|\mathbf{C}_N^\theta(\mathbf{r}) - \mathbf{C}_{GT}(\mathbf{r})\|^2 \quad (2)$$

where $r \in \mathcal{R}_b$ is a batch of rays sampled from the set of all rays.

3.2 Gaussian Submap

Multi-scale Gaussian Rendering Utilizing neural submap priors, we represent the scene using a set of anisotropic 3D Gaussian distributions. The scene is depicted as points associated with a position $p \in \mathbb{R}^3$, opacity $o \in [0, 1]$, third-order spherical harmonics (SH) coefficients $k \in \mathbb{R}^{16}$, a 3D scale $s \in \mathbb{R}^3$, and a 3D rotation $R \in SO(3)$ represented by a 4D quaternion $q \in \mathbb{R}^4$. \mathbf{c}_{GS} is the color value when rendering in 3D Gaussian. Inspired by equation (1), this representation can be rendered to a camera's image plane, with a correctly ordered list of points:

$$\mathbf{c}_{GS} = \sum_{j=1}^{N_p} \mathbf{c}_j \alpha_j T_{Gi} \quad \text{where } T_{Gi} = \prod_{i=1}^{j-1} (1 - \alpha_i) \quad (3)$$

Where T_{Gi} is the 3D Gaussian transmittance. Each Gaussian G_i contains optical properties: color \mathbf{c}_i and opacity α_i . For a continuous 3D representation, the mean \bar{x}_i and covariance \mathbf{T}_{CW} defined in world coordinates describe the Gaussian's location and its ellipsoidal shape. The 3D Gaussians $N(\bar{x}_W, \mathbf{Z}_W)$ in world coordinates are associated with 2D Gaussians $N(\bar{x}_I, \mathbf{Z}_I)$ on the image plane through the projection transformation:

$$\bar{x}_I = \pi(\mathbf{T}_{CW} \cdot \bar{x}_W), \quad \mathbf{Z}_I = \mathbf{J} \mathbf{W} \mathbf{Z}_W \mathbf{W}^T \mathbf{J}^T \quad (4)$$

\mathbf{W} is the rotational component of \mathbf{T}_{CW} , \mathbf{J} denotes the Jacobian of the affine approximation of the projective transformation [57], and \mathbf{Z}_W denotes the 3D covariance matrix. The radiance fields

provided by neural submaps serve as the foundational supervision for rendering, but they are prone to aliasing effects that degrade the rendering quality during the sampling process. This is particularly evident when constructing submaps with many small Gaussians, leading to severe artifacts. We employ a multi-scale Gaussian rendering approach inspired by [53], aggregating smaller Gaussians into larger ones to improve the rendering quality. We represent from Gaussian functions at four detail levels corresponding to $1\times$, $4\times$, $16\times$, and $64\times$ down-sampling resolutions. During the training process, smaller fine-level Gaussian functions are aggregated to create coarser-level larger Gaussians. The selection of Gaussians is based on pixel coverage, including or excluding according to the coverage range defined by the inverse of the highest frequency component in that region $f_{\max} = \frac{1}{S_k}$. Specifically, after performing global bundle adjustment, we do not perform additional Gaussians aggregation to ensure the stability of submap boundaries.

Ray-Guided Gaussian Pruning In order to reduce the number of ineffective Gaussians during Gaussian rendering and to improve the rendering speed, we adopted a pruning method in the Gaussian rendering process guided by ray sampling. We employed an importance assessment strategy to remove invalid points from all the Gaussians. The importance score is defined by the contribution of the aggregated Gaussians particles to the rays in all input images. To improve filtering efficiency, we introduced a sparse point cloud composed of ORB map points as guidance, which typically corresponds to regions near textured surfaces. Inspired by [6], we used a point cloud counter to gather statistics and counted rays with a number of nearby sparse points exceeding the threshold t_1 as the ray set K_r . The importance score can be expressed as:

$$\mathbf{E}(\mathbf{p}_i) = \max_{I_f \in \mathcal{I}_f, r \in I_f, r \in \mathbf{K}_r} (\alpha_i^r T_{Gi}^r) \quad (5)$$

where I_f is the rendered image and \mathcal{I}_f is the target image. $\alpha_i^r T_{Gi}^r$ represents the contribution of Gaussian \mathbf{p}_i to the final color prediction of a pixel along the ray, as described in equation (3). The mask values are computed as follows:

$$m_i = m(\mathbf{p}_i) = \mathbf{1}(\mathbf{E}(\mathbf{p}_i) < t_{\text{prune}}) \quad (6)$$

where $t_{\text{prune}} \in [0, 1]$ is a threshold used to control the number of points representing the scene. All Gaussians distributions with a mask value of 1 are removed from the scene. Finally, we execute default rasterization, ensuring that our rendering speed does not decrease and improving accuracy through pruning.

3.3 Loop Closure and BA

Local-Global Loop Closure To correct accumulative drift, we perform local Bundle Adjustment (BA) within each submap, involving only local submap keyframe corrections. Inspired by [30], we utilize the Bag of Words (BoW) model for relevance detection among global keyframes. When loop closure conditions are met, a global optimization process is initiated. To align global submaps and fuse submaps, we adopt a coarse-to-fine global adjustment strategy.

In contrast to traditional methods, we first optimize the pose of anchor frames using BA and perform a submap fusion process. This prevents drift at the boundaries of Gaussian submaps. Afterwards, we fix the position of anchor frames, execute a global BA process based on the global keyframe list, and then perform a second Gaussian submap fusion process to complete loop closure. This enables our system to correct significant drift while avoiding missing and overlapping artifacts caused by map misalignment. Additionally, we randomly sample rays from all keyframes involved in global BA to guide the generation and fusion of Gaussians, implementing the process described in Section 3.2 to further correct rendering errors.

Local-Global Bundle Adjustment Unlike methods that adjust using neural point clouds, our approach does not correct all mapping errors at once. Instead, we perform coarse-to-fine rendering adjustments. Thanks to the speed advantage of 3D Gaussian rendering, we can achieve real-time re-rendering and construct bundle adjustment (BA) losses.

To ensure geometric shape and appearance consistency, we distort the rendered RGB and depth to the co-visible keyframes, constructing the loss according to the following equations:

$$\mathcal{L}_{\text{BA-rgb}} = \sum_{i=1}^{N-1} \sum_{j=i+1}^N \left(\left| T_{Gi}^j \cdot \mathcal{R}(T_{Gi}, c) - F_{Gj}^c \right| \right) \quad (7)$$

$$\mathcal{L}_{\text{BA-depth}} = \sum_{i=1}^{N-1} \sum_{j=i+1}^N \left(\left| T_{Gi}^j \cdot \mathcal{R}(T_{Gi}, d) - F_{Gj}^d \right| \right) \quad (8)$$

where F_{Gj}^c and F_{Gj}^d are the color and depth of keyframe j , respectively. $\mathcal{R}(T_{Gi}, c)$ and $\mathcal{R}(T_{Gi}, d)$ represent the rendered RGB and depth. Thus, the overall loss function \mathcal{L}_{BA} used for joint optimization of the corresponding keyframe poses and 3D Gaussian scene representation is a weighted sum of the above losses. In our experiments, we found that the scale explosion of aggregated Gaussians during the BA process may affect rendering. Therefore, we apply an \mathcal{L}_2 loss \mathcal{L}_{rgs} to 3D Gaussians with scales exceeding the threshold t_2 . The total rendering loss \mathcal{L} we obtain is:

$$\mathcal{L}_{\text{BA}} = \lambda_1 \mathcal{L}_{\text{color}} + \lambda_2 \mathcal{L}_{\text{depth}} + \lambda_3 \mathcal{L}_{\text{rgs}} \quad (9)$$

Where λ_1 , λ_2 , and λ_3 are weighting coefficients. To address potential local errors caused by forgetting 3DGS submaps, we conduct extra optimization iterations for all co-visible keyframes. Unlike methods using neural point clouds, our approach benefits from faster rendering and lower computational costs of Gaussian rasterization. Unlike the high computational cost in [54], we avoid globally re-rendering neural radiation fields.

3.4 Submap Fusion

We represent the scene as the sum of multiple local scenes:

$$\{I_i, D_i\}_{i=1}^M \mapsto \{\text{SF}_{\sigma_1}^1, \text{SF}_{\sigma_2}^2, \dots, \text{SF}_{\sigma_n}^n\} \quad (10)$$

The series $\{I_i, D_i\}_{i=1}^M$ represents a sequence of RGB-D inputs, where $\text{SF}_{\sigma_n}^n$ denotes the submap representation. When generating a new submap, all submaps are anchored based on the spatial positions of local keyframe poses. After each local Bundle Adjustment (BA), the central pose of the map is adjusted for re-anchoring. To avoid overlapping artifacts at the edges of rendered submaps, we remove Gaussians outside all submap boundaries, effectively reducing boundary artifacts. Then, we proceed with submap fusion. After loop closure adjustment and global BA execution, we repeat the map fusion process. Our submap fusion strategy avoids excessive memory consumption caused by continuous map expansion. To ensure seamless map integration, we employ the Gaussian kernel aggregation method described in Section 3.2 after all submaps are fused. We observe that the merged boundaries are seamlessly connected.

4 Experiments

Implementation Details. We implemented NGM-SLAM on a desktop computer equipped with an Intel i7-12700K and an NVIDIA RTX 3090 Ti with 24 GB. Our implementation utilized mixed programming in C++ and Python. To ensure fair comparisons, we provided experimental data for both monocular and RGB-D setups. Detailed parameter settings are available in the supplementary materials. Our baselines include traditional methods, neural implicit approaches, and state-of-the-art (SOTA) systems based on 3D Gaussian SLAM, including ORBSLAM3 [30], BAD-SLAM [6], Vox-Fusion [39], DROID-SLAM [23], Co-SLAM [10], ESLAM [18], Go-SLAM [54], Point-SLAM [32], SplatAM [5] and MonoGS [4]. For some data, we used the results reported in the respective papers of these methodologies.

Datasets and Metrics. We utilized four RGB-D datasets, which include 8 small room sequences and 5 large-scale multi-room sequences from the Replica [3] dataset, featuring complex corridors and stairs. Additionally, we used 3 indoor scene sequences captured by real sensors from the TUM RGB-D [14] dataset, 6 sequences from the ScanNet [2] dataset, comprising large-scale real indoor scenes, 3 indoor scene sequences from the EuRoC [8] dataset, and 4 indoor sequences with challenging large perspective changes from the Openloris-Scene [31] dataset. For tracking, we employed ATE RMSE

(cm) as the benchmark. For reconstruction, we compared rendering accuracy using Depth L1(cm), PSNR, SSIM, and LPIPS. Our computational results represent the average of 5 experiments rendered along the camera’s direction for all frames. We assessed running speed and computational resource requirements using FPS and GPU Memory Usage.

4.1 Evaluation on Replica

Part	Apartment-0	Apartment-1	Apartmen-2	Frl-apartment-0	Frl-apartment-4	Average
NICE-SLAM [1]	16.99	14.52	8.19	3.99	4.31	9.60
Co-SLAM [10]	<u>8.60</u>	9.78	6.31	2.70	4.11	6.30
Go-SLAM [54]	14.10	3.54	<u>4.51</u>	<u>2.01</u>	2.30	<u>5.29</u>
Go-SLAM(Mono) [54]	29.81	17.43	8.99	11.77	14.42	14.48
SplaTAM [5]	20.33	10.97	8.22	6.03	10.49	10.55
MonoGS [4]	19.02	9.37	7.52	3.01	9.23	6.57
NGM-SLAM(Mono)	17.86	9.18	7.37	2.51	<u>1.98</u>	7.78
NGM-SLAM	5.23	<u>4.91</u>	2.62	2.01	<u>1.53</u>	3.26

Table 1: The performance of ATE RMSE (cm) on 5 large-scale scene sequences from the Replica [3] dataset. The average of 5 measurements is taken for each sequence. The best result is indicated in bold, and the second-best result is underlined. Our method outperformed the baseline method.

As shown in Table 1, we present the tracking results on 5 larger-scale scenes from the Replica [3] dataset. Our method’s ATE results show a 23.9% improvement in accuracy compared to Go-SLAM [54]. As illustrated in Fig 2, compared to the baseline method, we avoid the accumulation of errors caused by large-scale tracking. In complex large-scale scenes such as Apartment-1, which includes multiple rooms and corridors between rooms, accumulated errors can lead to catastrophic forgetting of the scene, highlighting the importance of loop closure. Meanwhile, we keep the advantages in detail representation.



Figure 2: In the Replica [3] dataset, we conducted reconstruction experiments on 5 large-scale apartment sequences with multiple rooms. The results demonstrate that our method achieves more accurate reconstruction and robust tracking compared to NeRF-based approaches and state-of-the-art methods based on 3DGS. Furthermore, our method avoids catastrophic forgetting and submap pose errors. This is particularly evident in the large-scale scene Apartment-0 with two floors.

As shown in Table 2, we provide experimental data for monocular and RGB-D small-scale room scenes, comparing them with other methods. We demonstrate the quality evaluation of scene reconstruction, including PSNR(dB), SSIM, LPIPS, ATE RMSE (cm) and the running speed. Our method achieves state-of-the-art results, which gives it an advantage over other 3DGS methods. Our monocular mode can also achieve reconstruction quality close to RGB-D without depth supervision. As shown in Fig 3, we compare the reconstruction results of monocular and RGB-D modes with other methods on room sequences from the Replica [3] dataset. To highlight our advantage in filling gaps, we compared our gap filling method with Co-SLAM which use the neural implicit representations.

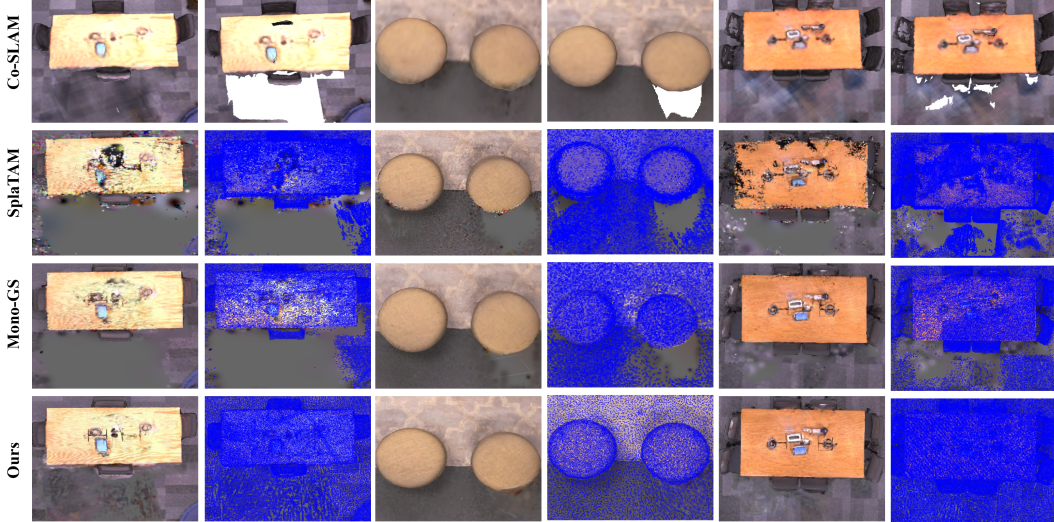


Figure 3: We present reconstruction and hole-filling results on three sequences in the Replica dataset [3]. Leveraging the prior information provided by our neural subgraphs, our method is capable of filling scene holes in a reasonable manner. This is crucial for achieving complete scene reconstruction, as we effectively generate dense Gaussians for completion while preserving the advantage in detail expression. Our Gaussians are sparser which is important to reduce rendering cost.

When Co-SLAM [10] does not completely fill these gaps, the resulting gaps resemble those from the unfilled 3DGS method. Our approach effectively fills these gaps or holes and generates dense Gaussian distributions. Moreover, compared to other methods, we exhibit superior performance in local details, with a more uniform Gaussian distribution at the same scale.

4.2 Evaluation on ScanNet

Our tracking results on the ScanNet [2] dataset are shown in Table 3. We demonstrate more robust tracking when loop closure detection and bundle optimization are enabled. In Fig 4, we illustrate the local reconstruction results, where our method can reasonably fill in gaps, such as chairs and walls. Additionally, by eliminating the accumulation errors in mapping and correcting mapping errors caused by incorrect scene updates, we can accurately recover the geometric shapes of objects, such as bicycles, shoes, and cellos in the scene.

Metrics	PSNR(dB) \uparrow	SSIM \uparrow	LPIPS \downarrow	ATE(cm) \downarrow	Tracking FPS \uparrow	System FPS \uparrow	GPU Usage(G) \downarrow
NICE-SLAM [1]	24.42	0.81	0.23	2.35	2.33	1.91	6.27
Co-SLAM [10]	24.15	0.77	0.35	1.12	10.74	8.26	14.44
Point-SLAM [32]	33.49	<u>0.97</u>	0.14	0.73	1.10	0.42	7.31
SplatTAM [5]	31.81	0.96	0.16	<u>0.55</u>	1.07	0.42	18.87
MonoGS [4]	34.05	0.96	<u>0.12</u>	0.58	4.58	2.26	27.99
NGM-SLAM(Mono)	<u>35.02</u>	0.96	0.13	8.51	<u>16.11</u>	3.82	7.62
NGM-SLAM	37.43	0.98	0.08	0.51	20.54	<u>5.71</u>	5.98

Table 2: The average results of 5 measurements for eight scenes of a sequence of smaller rooms in the Replica [3] dataset are reported for PSNR (dB), SSIM, LPIPS, ATE (cm), Tracking FPS, System FPS, and GPU usage. The best results are bolded, and the second best results are indicated with an underline.

Part	scene0000	scene0059	scene0106	scene0169	scene0181	scene0207	Average
NICE-SLAM [1]	8.64	12.25	8.09	10.28	12.93	5.59	9.63
Co-SLAM [10]	<u>7.13</u>	11.14	9.36	5.90	11.81	<u>7.14</u>	8.75
Vox-Fusion [39]	16.62	24.23	8.41	27.33	23.31	9.49	18.23
ESLAM [18]	7.54	8.52	7.39	8.17	9.13	5.61	<u>7.73</u>
Point-SLAM [32]	10.24	7.81	8.65	22.16	14.77	9.54	12.20
SplaTAM [5]	12.83	10.10	17.72	12.08	11.10	7.47	11.88
NGM-SLAM(w/o loop)	7.42	<u>6.43</u>	<u>7.31</u>	<u>6.81</u>	12.33	7.92	8.05
NGM-SLAM(w/ loop)	6.71	6.26	7.24	5.83	<u>10.12</u>	7.44	7.27

Table 3: The performance of ATE RMSE (cm) on 5 large-scale scene sequences from the Replica [3] dataset. The average of 5 measurements is taken for each sequence. The best result is indicated in bold, and the second-best result is underlined. Our method outperformed the baseline method.



Figure 4: On large-scale multi-room sequences in the ScanNet [2] dataset, our method demonstrates superior error accumulation correction capability compared to current NeRF/3DGS approaches. We can accurately ensure consistency across multiple views, avoiding erroneous scene reconstructions such as blurry shoes and bicycles, while also preventing local detail collapse caused by aliasing artifacts. Specifically, our method can run in real-time with only 8GB GPU memory usage and 5.4FPS in the large scenes of ScanNet [2].

5 Conclusion

We propose NGM-SLAM, the first Gaussian SLAM system based on neural radiance field submaps. Through the priors provided by submaps and loop closure adjustments, we achieve high-quality tracking and reconstruction of large-scale scenes, enabling local-to-global loop closures and correcting cumulative errors. We strike a balance between high-quality texture detail representation and real-time operation. Experimental results demonstrate that our approach outperforms state-of-the-art NeRF/GS-based SLAM methods in terms of rendering and tracking accuracy. In the future, our system may be expanded to dynamic scenarios and extremely large-scale environments.

References

- [1] T. Pire, T. Fischer, G. Castro, P. De Crist'oforis, J. Civera, and J. J. Berles. S-PTAM: Stereo parallel tracking and mapping. *Robotics and Autonomous Systems*, 93:27–42, 2017.
- [2] S. Zakharov, W. Kehl, A. Bhargava, and A. Gaidon. Autolabeling 3d objects with differentiable rendering of sdf shape priors. In *Proceedings of the IEEE/CVF Conference on Computer Vision and Pattern Recognition*, pages 12224–12233, 2020.
- [3] Chen Wang, Xian Wu, Yuan-Chen Guo, Song-Hai Zhang, Yu-Wing Tai, and Shi-Min Hu. NeRF-SR: High Quality Neural Radiance Fields using Supersampling. In *Proceedings of the 30th ACM International Conference on Multimedia*, pages=6445–6454, 2022.
- [4] Jeffrey Ichniowski, Yahav Avigal, Justin Kerr, and Ken Goldberg. Dex-nerf: Using a neural radiance field to grasp transparent objects. *arXiv preprint arXiv:2110.14217*, 2021.
- [5] Benran Hu, Junkai Huang, Yichen Liu, Yu-Wing Tai, and Chi-Keung Tang. NeRF-RPN: A general framework for object detection in NeRFs. *arXiv preprint arXiv:2211.11646*, 2022.
- [6] Thomas Schops, Torsten Sattler, and Marc Pollefeys. Bad slam: Bundle adjusted direct RGB-D slam. In *Proceedings of the IEEE/CVF Conference on Computer Vision and Pattern Recognition*, pages=134–144, 2019.
- [7] Z. Zhu, S. Peng, V. Larsson, et al., “Nicer-slam: Neural implicit scene encoding for RGB SLAM,” *arXiv preprint arXiv:2302.03594*, 2023.
- [8] M. Burri, J. Nikolic, P. Gohl, et al. "The EuRoC micro aerial vehicle datasets," *The International Journal of Robotics Research*, vol. 35, no. 10, pp. 1157-1163, 2016.
- [9] Z. Zhu, S. Peng, V. Larsson, W. Xu, H. Bao, Z. Cui, M. R. Oswald, and M. Pollefeys, "Nice-slam: Neural implicit scalable encoding for slam," in *Proceedings of the IEEE/CVF Conference on Computer Vision and Pattern Recognition*, 2022, pp. 12786–12796.
- [10] Hengyi Wang, Jingwen Wang, Lourdes Agapito. "Co-SLAM: Joint Coordinate and Sparse Parametric Encodings for Neural Real-Time SLAM," in *Proceedings of the IEEE/CVF Conference on Computer Vision and Pattern Recognition (CVPR)*, 2023, pp. 13293-13302.
- [11] A. Dai, A. X. Chang, M. Savva, M. Halber, T. Funkhouser, and M. Nießner, "Scannet: Richly-annotated 3d reconstructions of indoor scenes," in *Proceedings of the IEEE Conference on Computer Vision and Pattern Recognition*, 2017, pp. 5828–5839.
- [12] J. Huang, S.-S. Huang, H. Song, and S.-M. Hu. "Di-fusion: Online implicit 3d reconstruction with deep priors," in *Proceedings of the IEEE/CVF Conference on Computer Vision and Pattern Recognition*, 2021, pp. 8932–8941.
- [13] J. Straub, T. Whelan, L. Ma, Y. Chen, E. Wijmans, S. Green, J.J. Engel, R. Mur-Artal, C. Ren, S. Verma, et al. "The Replica Dataset: A digital replica of indoor spaces," *arXiv preprint arXiv:1906.05797*, 2019.
- [14] J. Sturm, W. Burgard, and D. Cremers. "Evaluating egomotion and structure-from-motion approaches using the TUM RGB-D benchmark," in *Proc. of the Workshop on Color-Depth Camera Fusion in Robotics at the IEEE/RJS International Conference on Intelligent Robot Systems (IROS)*, 2012, pp. 1–7.
- [15] R.A. Newcombe, S.J. Lovegrove, and A.J. Davison. "DTAM: Dense tracking and mapping in real-time," in *2011 International Conference on Computer Vision*, IEEE, 2011, pp. 2320–2327.
- [16] R. Mur-Artal, J.M.M. Montiel, and J.D. Tardos. "ORB-SLAM: a versatile and accurate monocular SLAM system," *IEEE Transactions on Robotics*, vol. 31, no. 5, pp. 1147–1163, 2015.
- [17] Z. Liao, Y. Hu, J. Zhang, X. Qi, X. Zhang, and W. Wang. "So-slam: Semantic object slam with scale proportional and symmetrical texture constraints," *IEEE Robotics and Automation Letters*, vol. 7, no. 2, pp. 4008–4015, 2022.
- [18] Johari, M. M., Carta, C., Fleuret, F. "ESLAM: Efficient Dense SLAM System Based on Hybrid Representation of Signed Distance Fields." In *Proceedings of the IEEE/CVF Conference on Computer Vision and Pattern Recognition (CVPR)*, 2023.
- [19] M. R"unz and L. Agapito, “Co-fusion: Real-time segmentation, tracking and fusion of multiple objects,” in *2017 IEEE International Conference on Robotics and Automation (ICRA)*, 2017, pp. 4471–4478.

- [20] Michael Bloesch, Jan Czarnowski, Ronald Clark, Stefan Leutenegger, and Andrew J Davison. "CodeSLAM—learning a compact, optimisable representation for dense visual SLAM." In *Proceedings of the IEEE Conference on Computer Vision and Pattern Recognition*, pp. 2560-2568. 2018.
- [21] R. Craig and R. C. Beavis, "TANDEM: matching proteins with tandem mass spectra," *Bioinformatics*, vol. 20, no. 9, pp. 1466–1467, 2004.
- [22] Y. Yao, Z. Luo, S. Li, T. Shen, T. Fang, and L. Quan, "Recurrent MVSNet for high-resolution multi-view stereo depth inference," in *Proceedings of the IEEE/CVF Conference on Computer Vision and Pattern Recognition*, 2019, pp. 5525–5534.
- [23] Z. Teed and J. Deng, "Droid-slam: Deep visual slam for monocular, stereo, and RGB-D cameras," *Advances in Neural Information Processing Systems*, vol. 34, pp. 16558-16569, 2021.
- [24] A. Yu, V. Ye, M. Tancik, and A. Kanazawa, "Pixelnerf: Neural radiance fields from one or few images," in *Proceedings of the IEEE/CVF Conference on Computer Vision and Pattern Recognition*, 2021, pp. 4578-4587.
- [25] Kangle Deng, Andrew Liu, Jun-Yan Zhu, and Deva Ramanan, "Depth-supervised NeRF: Fewer views and faster training for free," in *Proceedings of the IEEE/CVF Conference on Computer Vision and Pattern Recognition*, 2022, pp. 12882-12891.
- [26] Y.-C. Guo, D. Kang, L. Bao, Y. He, and S.-H. Zhang, "Nerfren: Neural radiance fields with reflections," in *Proceedings of the IEEE/CVF Conference on Computer Vision and Pattern Recognition*, 2022, pp. 18409-18418.
- [27] Q. Xu, Z. Xu, J. Philip, S. Bi, Z. Shu, K. Sunkavalli, and U. Neumann. "Point-nerf: Point-based neural radiance fields," in *Proceedings of the IEEE/CVF Conference on Computer Vision and Pattern Recognition*, 2022, pp. 5438-5448.
- [28] J. T. Barron, B. Mildenhall, M. Tancik, P. Hedman, R. Martin-Brualla, and P. P. Srinivasan, "Mip-nerf: A multiscale representation for anti-aliasing neural radiance fields," in *Proceedings of the IEEE/CVF International Conference on Computer Vision*, 2021, pp. 5855–5864.
- [29] Bernhard Kerbl, et al., "3D Gaussian Splatting for Real-Time Radiance Field Rendering," *ACM Transactions on Graphics (ToG)*, 42.4 (2023): 1-14.
- [30] C. Campos, R. Elvira, J. J. G. Rodríguez, J. M. M. Montiel, and J. D. Tardós, "ORB-SLAM3: An Accurate Open-Source Library for Visual, Visual-Inertial, and Multimap SLAM," *IEEE Transactions on Robotics*, vol. 37, no. 6, pp. 1874–1890, 2021.
- [31] Shi, X., Li, D., Zhao, P., et al., "Are we ready for service robots? The OpenLORIS-Scene datasets for lifelong SLAM," In *Proceedings of the 2020 IEEE International Conference on Robotics and Automation (ICRA)*, IEEE, 2020, pp. 3139-3145.
- [32] Erik Sandström, Yanchao Li, Luc Van Gool, et al., "Point-SLAM: Dense Neural Point Cloud-Based SLAM," in *Proceedings of the IEEE/CVF International Conference on Computer Vision*, 2023, pp. 18433-18444.
- [33] T. Whelan, M. Kaess, M. Fallon, H. Johannsson, J. Leonard, and J. McDonald, "Kintinuous: Spatially extended kinectfusion," in *Proc. Workshop RGB-D, Adv. Reason. Depth Cameras*, 2012, article 4.
- [34] T. Deng, H. Xie, J. Wang, W. Chen. "Long-Term Visual Simultaneous Localization and Mapping: Using a Bayesian Persistence Filter-Based Global Map Prediction," *IEEE Robotics & Automation Magazine*, vol. 30, no. 1, pp. 36-49, 2023.
- [35] T. Deng, G. Shen, T. Qin, J. Wang, W. Zhao, J. Wang, D. Wang, W. Chen. "PLGSLAM: Progressive Neural Scene Representation with Local to Global Bundle Adjustment," *arXiv preprint arXiv:2312.09866*, 2023.
- [36] T. Deng, S. Liu, X. Wang, Y. Liu, D. Wang, W. Chen. "ProSGNeRF: Progressive Dynamic Neural Scene Graph with Frequency Modulated Auto-Encoder in Urban Scenes," *arXiv preprint arXiv:2312.09076*, 2023.
- [37] T. Qin, P. Li, S. Shen. "Vins-mono: A robust and versatile monocular visual-inertial state estimator," *IEEE Transactions on Robotics*, vol. 34, no. 4, pp. 1004-1020, 2018.
- [38] T. Whelan, M. Kaess, H. Johannsson, et al. "Real-time large-scale dense RGB-D SLAM with volumetric fusion," *The International Journal of Robotics Research*, vol. 34, no. 4-5, pp. 598-626, 2015.

- [39] X. Yang, H. Li, H. Zhai, et al., "Vox-Fusion: Dense tracking and map with voxel-based neural implicit representation," in *2022 IEEE International Symposium on Mixed and Augmented Reality (ISMAR)*, IEEE, 2022, pp. 499-507.
- [40] M. Hosseinzadeh, K. Li, Y. Latif, et al. "Real-time monocular object-model aware sparse SLAM," in *2019 International Conference on Robotics and Automation (ICRA)*, IEEE, 2019, pp. 7123-7129.
- [41] T. Qin, P. Li, S. Shen, "Vins-mono: A robust and versatile monocular visual-inertial state estimator," *IEEE Transactions on Robotics*, 34(4): 1004-1020, 2018.
- [42] Hidenobu Matsuki, Riku Murai, Paul H. J. Kelly, Andrew J. Davison, "Gaussian Splatting SLAM," in *Proceedings of the IEEE/CVF Conference on Computer Vision and Pattern Recognition*, 2024.
- [43] Chi Yan, Delin Qu, Dan Xu, Bin Zhao, Zhigang Wang, Dong Wang, Xuelong Li, "GS-SLAM: Dense Visual SLAM with 3D Gaussian Splatting," in *CVPR*, 2024.
- [44] X. Kong, S. Liu, M. Taher, et al., "vmap: Vectorised object map for neural field slam," in *Proceedings of the IEEE/CVF Conference on Computer Vision and Pattern Recognition*, 2023, pp. 952-961.
- [45] M. Li, J. He, Y. Wang, et al. "End-to-End RGB-D SLAM With Multi-MLPs Dense Neural Implicit Representations," *IEEE Robotics and Automation Letters*, 2023.
- [46] C. M. Chung, Y. C. Tseng, Y. C. Hsu, et al., "Orbeez-SLAM: A Real-Time Monocular Visual SLAM with ORB Features and NeRF-Realized Map," in *2023 IEEE International Conference on Robotics and Automation (ICRA)*, IEEE, 2023, pp. 9400-9406.
- [47] R. A. Newcombe, S. Izadi, O. Hilliges, D. Molyneaux, D. Kim, A. J. Davison, P. Kohi, J. Shotton, S. Hodges, and A. Fitzgibbon, "Kinectfusion: Real-time dense surface mapping and tracking," in *2011 10th IEEE international symposium on mixed and augmented reality*, 2011, pp. 127-136.
- [48] E. Sucar, S. Liu, J. Ortiz, and A. J. Davison, "iMAP: Implicit mapping and positioning in real-time," in *Proceedings of the IEEE/CVF International Conference on Computer Vision*, 2021, pp. 6229–6238.
- [49] A. Rosinol, J. J. Leonard, and L. Carlone, "NeRF-SLAM: Real-Time Dense Monocular SLAM with Neural Radiance Fields," *arXiv preprint arXiv:2210.13641*, 2022.
- [50] T. Müller, A. Evans, C. Schied, and A. Keller, "Instant neural graphics primitives with a multiresolution hash encoding," *ACM Transactions on Graphics (ToG)*, vol. 41, no. 4, pp. 1–15, 2022.
- [51] P. Wang, L. Liu, Y. Liu, C. Theobalt, T. Komura, and W. Wang, "Neus: Learning neural implicit surfaces by volume rendering for multi-view reconstruction," *arXiv preprint arXiv:2106.10689*, 2021.
- [52] H. Turki, D. Ramanan, and M. Satyanarayanan, "Mega-nerf: Scalable construction of large-scale nerfs for virtual fly-throughs," in *Proceedings of the IEEE/CVF Conference on Computer Vision and Pattern Recognition*, 2022, pp. 12922–12931.
- [53] Zehao Yu, Torsten Sattler, Andreas Geiger, "Gaussian Opacity Fields: Efficient High-quality Compact Surface Reconstruction in Unbounded Scenes," *arXiv:2404.10772*, 2024.
- [54] Y. Zhang, F. Tosi, S. Mattoccia, et al. "Go-slam: Global optimization for consistent 3D instant reconstruction," in *Proceedings of the IEEE/CVF International Conference on Computer Vision*, 2023, pp. 3727-3737.
- [55] Nikhil Keetha, Jay Karhade, Krishna Murthy Jatavallabhula, Gengshan Yang, Sebastian Scherer, Deva Ramanan, Jonathon Luiten, "SplaTAM: Splat, Track & Map 3D Gaussians for Dense RGB-D SLAM," in *Proceedings of the IEEE/CVF Conference on Computer Vision and Pattern Recognition*, 2024.
- [56] M. Niemeyer, F. Manhardt, M. J. Rakotosaona, et al. *RadSplat: Radiance Field-Informed Gaussian Splatting for Robust Real-Time Rendering with 900+ FPS*. *arXiv preprint arXiv:2403.13806*, 2024.
- [57] M. Zwicker, H. Pfister, J. Van Baar, et al. *EWA volume splatting*. In *Proceedings Visualization*, 2001. VIS'01. IEEE, 2001, pp. 29-538.
- [58] C. Forster, Z. Zhang, M. Gassner, M. Werlberger, and D. Scaramuzza. *SVO: Semidirect visual odometry for monocular and multicamera systems*. *IEEE Transactions on Robotics*, 33(2):249–265, 2016.
- [59] Huang, Huajian, Li, Longwei, Cheng Hui, and Yeung, Sai-Kit. "Photo-SLAM: Real-time Simultaneous Localization and Photorealistic Mapping for Monocular, Stereo, and RGB-D Cameras." In *Proceedings of the IEEE/CVF Conference on Computer Vision and Pattern Recognition*, 2024.

-Supplementary Material-

In the supplementary materials, in Sec. A we present additional experimental details. In Sec. B, we provide the results of ablation experiments. In Sec. C, we present additional experimental results, including a large-scale synthetic dataset with 11 rooms and a real-world apartment scene with 5 rooms. In Sec. D we discussed the limitations of the paper.

A Implementation Details

Relative to the current 3DGS-SLAM system, NGM-SLAM can run in real-time on platforms with a minimum of 6GB of GPU memory usage. To ensure the submap creation process is sufficiently reasonable and to prevent errors caused by overly small submaps during scene optimization, we set the initial submap threshold N to 200. We set the threshold t_1 for ray sampling counters to 5. The threshold t_{prune} which is used to control the number of points representing the scene, is initially set to 0.01. The threshold t_2 , controlling the size of 3DGS, is set to 10. The loss functions L_1 , L_2 , and L_3 , used for participating in BA optimization, are initialized to 0.005, 1, and 1.

B Ablation Study

Gaussian Primitives Pruning In Fig 5, we present comparative results of Gaussian body pruning [6] guided by point clouds against other methods on the Apartment-1 and room-0 sequences in Replica [3]. In Fig 5, we illustrate the results on the apartment-1 sequence, where a balance between runtime speed and reconstruction accuracy is achieved at 7000 iterations. Our experimental findings on the room0 sequence are depicted in Table 6. Beyond 7000 iterations, there is a marginal improvement in system reconstruction accuracy but a notable decrease in FPS. Additionally, if the pruning strategy from MonoGS [4] is adopted, we observe a decline in reconstruction quality and speed. This is primarily because methods solely based on viewing from common perspectives cannot accurately prune the point clouds provided by neural submap. In smaller scenes, our method exhibits a 12% speed enhancement compared to the original unpruned version, while in larger scenes, this advantage expands to 27%.

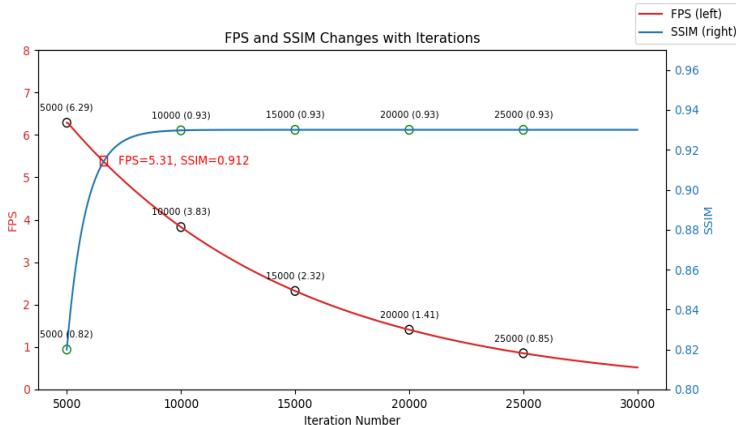


Figure 5: The reconstruction results of SplaTAM [5] compared to anchor frame BA and full global BA strategies on the apartment-1 sequence in Replica.

	w/o pruning	w pruning(iter=7000)	w pruning(iter=30000)	w pruning(Mono-GS)
FPS↑	5.13	5.74	2.19	<u>5.31</u>
SSIM↑	0.92	<u>0.96</u>	0.97	0.95

Table 4: Results on room0 sequence. The best results are indicated in bold, the second-best results are indicated with an underline. We chose 7,000 iterations to balance real-time performance and reconstruction results.

Neural Submap In Table 7, We presented the results of the ablation experiment on the Apartment-0 sequence from the Replica dataset [3]. Including the differences in mapping quality and speed between using different neural subgraphs and conventional point cloud subgraphs representations. It can be observed that employing the Instant-NGP encoding method leads to relatively faster speed and higher reconstruction quality. Additionally, compared to traditional point cloud methods, it also exhibits significant advantages in terms of memory usage.

	w/o submap	Points cloud submap	One_blob submap	Instant_NGP submap
PSNR(dB)↑	17.22	30.15	<u>33.62</u>	33.83
FPS↑	2.42	1.13	<u>4.38</u>	5.69
ATE RMSE(cm)↓	6.71	<u>5.26</u>	7.24	5.23

Table 5: The best results are indicated in bold, the second-best results are indicated with an underline. Our approach can achieve optimal performance without compromising reconstruction quality.

Bundle Adjustment strategy We compared the reconstruction and tracking accuracy variations corresponding to different BA strategies on the Apartment-1 sequence from the Replica dataset [3]. In Fig. 6, we present the reconstruction results of SplaTAM [5] without any loop closure correction, revealing a noticeable map drift. Without submap anchor frame correction, there is map offsetting, and solely performing anchor frame correction fails to rectify the detail errors caused by cumulative errors, resulting in artifacts. Our strategy significantly corrects the accumulated errors in map pose and texture details. In Table 8, we illustrate the variations in PSNR (dB) and ATE RMSE (cm) with different strategies. Submap BA denotes the strategy employing only anchor frame correction, indicating that solely using anchor frame correction partially rectifies map errors. However, our submap-global BA approach effectively corrects cumulative errors entirely, maintaining robustness even in larger-scale scenarios.



Figure 6: The reconstruction results of SplaTAM [5], only local BA, local BA & anchor frame BA and full global BA strategies on the Apartment-1 sequence in Replica. Specifically, if we only perform global BA, it may result in the submaps being unable to align properly.

	w/o BA	only/ local BA	only/ submap BA	w/ local&submap BA	w/ full BA
PSNR(dB)↑	17.22	24.10	21.02	<u>25.36</u>	34.01
ATE RMSE(cm)↓	18.73	12.99	14.71	<u>5.64</u>	4.91

Table 6: The best results are indicated in bold, the second-best results are indicated with an underline. Without the submap BA strategy will result in submap pose offset.

Bundle Adjustment Loss We demonstrated the impact of different BA strategies on the results of the Replica Apartment-2 sequence as shown in Table 9. When applying depth and color loss, the PSNR improved by 24.3% compared to the unoptimized scenario. When only applying Gaussian scale loss, the PSNR improved by 3.1% compared to the unoptimized scenario. Although the improvement on the surface may not be significant, avoiding local scale explosions plays a crucial role in constraining local Gaussian errors, preventing the occurrence of radial artifacts in local Gaussians, which would significantly degrade scene quality. This is evident in the 2D metric (Depth L1), where the enhancement of 2D metrics proves that we have increased the consistency of the surface, avoiding rendering issues caused by local Gaussian scale explosions.

	w/o BA loss	w/ depth & color loss	w/ gaussian scale loss	w/ full loss
PSNR(dB)↑	26.23	<u>32.53</u>	27.02	34.77
Depth L1(cm)↓	1.82	1.62	<u>0.98</u>	0.81

Table 7: The best results are indicated in bold, the second-best results are indicated with an underline. Our approach can achieve optimal performance without compromising reconstruction quality.

C Additional Experiments

C.1 More results on the virtual synthetic dataset

We present the reconstruction results on the Apartment-0 sequence of the synthetic apartment dataset Replica[3] in Fig 7 and Fig 8, which includes two bathrooms, three bedrooms on the second floor, a living room, a kitchen, a study room on the ground floor, and a larger staircase area. This represents a challenging large-scale scene, and we have successfully completed the reconstruction task while maintaining good detail, with only minor localized mapping errors.



Figure 7: The reconstruction results of the first floor of the Apartment-0 sequence in Replica[3] dataset show the robustness of our method, achieving accurate reconstruction of details and shapes.



Figure 8: The reconstruction results for the second floor and overall reconstruction of the Apartment-0 sequence from the Replica dataset [3] demonstrate the robustness of our tracking against substantial rotations, particularly evident in areas like staircases. Moreover, our use of submap reconstruction effectively reduces GPU memory usage, preventing exponential growth as scene complexity expands. This feature is vital for applications in large scene reconstruction. Our approach achieves better results by avoiding the common pitfalls of existing NeRF and 3DGS-based methods, which often struggle to track and effectively reconstruct in such large-scale scenes.

We demonstrate the reconstruction results on four smaller scene sequences in Replica[3] dataset in Fig 9. Compared to other methods based on NeRF/GS, our approach provides more accurate reconstruction of details and is able to display finer textures.



Figure 9: The reconstruction results of the office-0, office-2, office-3 and room-0 sequence in Replica [3] dataset achieving accurate reconstruction of details and shapes.



Figure 10: Our method is capable of tracking in challenging environments and maintains robustness against complex lighting variations.

C.2 More results on the real-world dataset

We demonstrated the reconstruction results on real-world scenes in Fig 10, including the reconstruction results of a large-scale scene with 5 rooms from the NICE-SLAM [1] open-source dataset and the results of 6 sequence from the ScanNet [2] dataset. This illustrates the advantages of our approach at both large and local scales, as well as showcasing the generalization capability of our method, which can adapt to various types of scenes.



Figure 11: The dataset is from a large apartment with 5 rooms, open-sourced by NICE-SLAM [1]. In real-world scenarios, our submap strategy effectively corrected cumulative errors and achieved high-quality reconstruction.

C.3 Evaluation on TUM RGB-D and EuRoC

Our ATE RMSE (cm) and construction results in indoor scenes for TUM RGB-D[14] datasets as shown in Tables 4 and EuRoC [8] dataset in Tables 5. Our method achieves competitive results compared to traditional approaches in tracking performance.

	fr1_desk	fr2_xyz	fr3_office	AVG
DI-Fusion [12]	4.4	2.0	5.8	4.1
BAD-SLAM [6]	1.7	1.1	1.7	1.5
ESLAM [18]	2.3	1.1	2.4	2.0
MonoGS [4]	1.52	1.58	1.65	1.58
NGM-SLAM(Mono)	1.73	<u>0.72</u>	<u>1.42</u>	<u>1.29</u>
NGM-SLAM	<u>1.72</u>	0.40	1.00	1.04

Table 8: The performance of ATE RMSE (cm) on TUM RGB-D [14] dataset. The best result is indicated in bold, and the second-best result is underlined.

	V101	V102	V103	AVG
ORB-SLAM2 [16]	0.035	0.020	0.048	0.034
ORB-SLAM3 [30]	0.035	0.025	0.052	0.037
SVO [58]	0.045	0.040	0.070	0.051
Go-SLAM [54]	0.041	0.040	0.024	0.035
DROID-SLAM [23]	<u>0.037</u>	0.026	<u>0.023</u>	0.029
NGM-SLAM	0.033	<u>0.027</u>	0.020	0.027

Table 9: The performance of ATE RMSE (cm) for stereo input on the EuRoC [8] dataset, with the best result indicated in bold and the second-best result underlined.

Our reconstruction results on the ScanNet dataset are shown in Fig 11. Our method demonstrates excellent inpainting ability and scene generalization, especially compared to existing 3DGs methods. Due to our strong prior input, our approach exhibits robustness in representing complex scenes, accurately rendering them with a better sense of realism, and avoiding the generation of numerous Gaussian noise points.

The reconstruction results of four office sequences in the challenging Openloris-scene dataset as shown in Fig 12 which demonstrate the stability of our method under significant viewpoint changes, while preserving consistent representation of texture details.

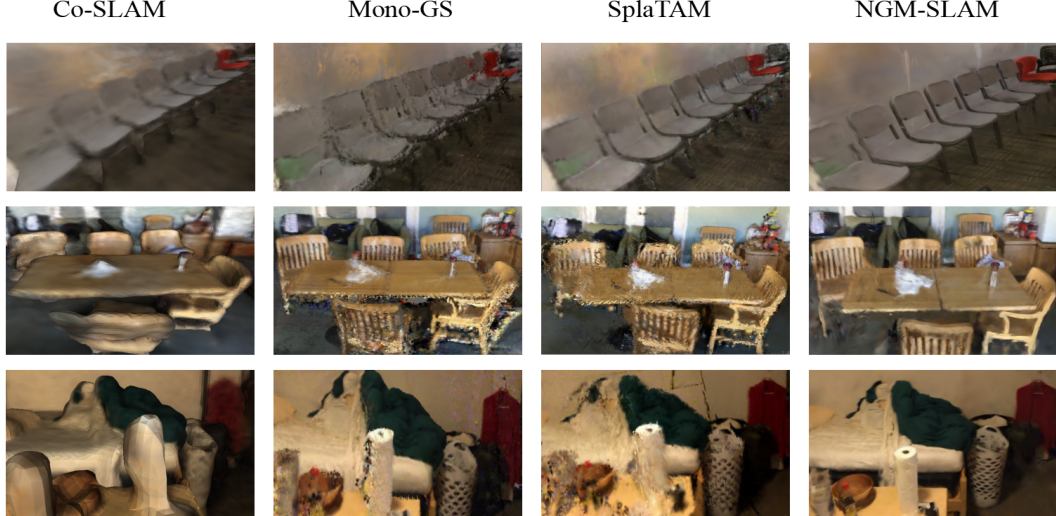


Figure 12: The reconstruction results on the ScanNet dataset show that our method is more robust compared to the GS-SLAM approach. Additionally, our method exhibits greater accuracy in handling complex real-world textures and reconstructing fine details. Furthermore, we mitigate local reconstruction errors and Gaussian scale explosions.

D Limitations

Although our system achieves state-of-the-art tracking and reconstruction results, we are limited by the current memory and computational resources, preventing us from achieving real-time reconstruction in large-scale scenes such as city-level scenarios. Our method can be ported to CUDA programming in the future, which will enhance the extraction of meshes and obtain high-quality mesh.

References

- [1] Z. Zhu, S. Peng, V. Larsson, W. Xu, H. Bao, Z. Cui, M. R. Oswald, and M. Pollefeys, "Nice-slam: Neural implicit scalable encoding for slam," in *Proceedings of the IEEE/CVF Conference on Computer Vision and Pattern Recognition*, 2022, pp. 12786–12796.
- [2] A. Dai, A. X. Chang, M. Savva, M. Halber, T. Funkhouser, and M. Nießner, "Scannet: Richly-annotated 3d reconstructions of indoor scenes," in *Proceedings of the IEEE Conference on Computer Vision and Pattern Recognition*, 2017, pp. 5828–5839.
- [3] J. Straub, T. Whelan, L. Ma, Y. Chen, E. Wijmans, S. Green, J.J. Engel, R. Mur-Artal, C. Ren, S. Verma, et al. "The Replica Dataset: A digital replica of indoor spaces," *arXiv preprint arXiv:1906.05797*, 2019.
- [4] Hidenobu Matsuki, Riku Murai, Paul H. J. Kelly, Andrew J. Davison, "Gaussian Splatting SLAM," in *Proceedings of the IEEE/CVF Conference on Computer Vision and Pattern Recognition*, 2024.
- [5] Nikhil Keetha, Jay Karhade, Krishna Murthy Jatavallabhula, Gengshan Yang, Sebastian Scherer, Deva Ramanan, Jonathon Luiten, "SplaTAM: Splat, Track & Map 3D Gaussians for Dense RGB-D SLAM," in *Proceedings of the IEEE/CVF Conference on Computer Vision and Pattern Recognition*, 2024.
- [6] M. Niemeyer, F. Manhardt, M. J. Rakotosaona, et al. *RadSplat: Radiance Field-Informed Gaussian Splatting for Robust Real-Time Rendering with 900+ FPS*. arXiv preprint arXiv:2403.13806, 2024.